47th AIAA/ASME/SAE/ASEE Joint Propulsion Conference & Exhibit
31 July - 03 August 2011, San Diego, California

AIAA 2011-5655

Investigation of Pre-ionization Characteristics in Heavy Gas Pulsed Inductive Plasmas via Numerical Modeling

Warner C. Meeks,[1] Ryan A. Pahl,[2] and Joshua L. Rovey[3]
Missouri University of Science and Technology, Rolla, Missouri 65409-0050

A globally-averaged, pulsed inductive plasma model is reproduced and utilized to investigate pre-ionization conditions for a pulsed inductive plasma accelerator. Attention is given to better quantifying the formation and energy conversion/loss processes associated with the pre-ionization stage. Simulations are completed for different power input pulse duration, seed plasma density, and total input energy. Results are analyzed based on the ion energy fraction and peak ion density. Ion energy fraction is the percentage of total input energy contained in ionization. Analysis shows that reducing pulse duration from 10^{-6} to 10^{-7} seconds increases ion energy fraction by 16.5%. Reducing pulse duration further to 10^{-8} seconds increases ion energy fraction only another 2.5%. The optimum pulse duration from these simulations is 200 ns because this duration maximizes both ion energy fraction and peak ion density. Results show that a low seed plasma density, less than 10^{14} m^{-3}, yields the highest ion energy fraction of 40%. Increasing seed plasma density above 10^{14} m^{-3} increases peak ion density but causes a corresponding decrease in ion energy fraction. Increasing total energy deposition from 5 to 160 mJ increases ion energy fraction from 33 to 58% at a 200 ns pulse duration. However this increase is not linear, but has a diminishing return with ion energy fraction plateau estimated to be 65%.

Nomenclature

e	fundamental charge (C)	n_{ground}	number density of ground state atoms (m^{-3})
E_i	energy for i^{th} collision reaction (V)	n_{ion}	ion number density (m^{-3})
$E_{induced}$	induced electric field (V m^{-1})	P_{abs}	total power absorbed by plasma formation
I_{sp}	specific impulse (s)	R	characteristic radius of cylindrical reactor (m)
k	Boltzmann's constant (J K^{-1})	T_e	electron temperature (V)
L	characteristic length of cylindrical reactor (m)	V	characteristic volume (m^3)
M	neutral mass (kg)	V_s	voltage potential across sheath (V)
K_i	rate constant for the i^{th} reaction	ε_0	permittivity of free space (C^2-s^2 kg^{-1} m^{-3})
P_{elec}	total electric power delivered to thrust device	ε_{ex}	average excitation energy (V)
A_{eff}	effective Einstein coefficient	ε_{iz}	ionization energy (V)
m	electron mass (kg)	η_t	thruster efficiency
n_e	electron number density (m^{-3})	λ_i	ion-neutral collision mean free path (m)
n_{ex}	number density excited state (m^{-3})	μ_0	permeability of free space (m-kg C^{-2})

I. Introduction

PULSED inductive plasmas (PIPs) have shown increased potential in multiple disciplines over the past twenty to thirty years. Applications ranging from surface etching of micro-finishes, to space propulsion concepts for long duration in both near-earth and interplanetary missions, to alternative fuel deposition methods in state-of-the-art nuclear fusion research have all cited an increased need for high performance induction plasmas.[1,2,3,4,5,6,7] The most appealing aspect by far of PIPs over more conventional ionization techniques is a lack of electrodes and hence a break from the concern over electrode erosion. Common practice is, in fact, to isolate the induction coil from the plasma discharge chamber via a dielectric barrier such as glass, quartz, or high-grade polymer.[8,9] This results in greatly improved device lifetime. The driving factor for continued research into these devices has been the desire

[1] Graduate Research Student, Mechanical and Aerospace Engineering, wcm994@mst.edu, AIAA Student Member.
[2] Graduate Research Student, Mechanical and Aerospace Engineering, rap4yd@mst.edu, AIAA Student Member.
[3] Assistant Professor, Mechanical and Aerospace Engineering, roveyj@mst.edu, AIAA Senior Member.

for increasingly higher density plasmas with minimum input power.

PIP accelerators (PIPAs) have seen a great deal of development over the past 2-3 decades in their application to aerospace electric propulsion (EP). A number of these EP concepts have been bench-tested including the Pulsed Inductive Thruster (PIT) developed by NASA and Northrop Grumman,[10,11,12] the Plasmoid Thruster Experiment (PTX) researched at Univ. of Alabama-Huntsville,[13] the Electrodeless Lorentz Force (ELF) thruster researched by Univ. of Washington,[14] the Experimental Coaxial Field Reversed Configuration Thruster (XOCOT) researched by AFRL-Edwards AFB,[8] and the Faraday Accelerator with Radio-frequency-Assisted Discharge (FARAD) researched at Princeton's EPPDyL.[15] PIT has been investigated since the early 1980's by NASA and has seen multiple iterations and refinements. The PIT device is generally characterized by a planar coil geometry and a formation and acceleration time of 10-20 μs. PTX is primarily characterized by the formation of field-reversed configuration (FRC) plasmas with a purely poloidal, self-consistent (i.e., closed) magnetic field facilitated by a cylindrical induction coil. The ELF thruster has a reasonable taper to the coil yielding a more conical geometry. This provides an inherent acceleration mechanism for the FRC by way of an asymmetric magnetic field. Also the ELF thruster utilizes a rotating magnetic field (RMF) for plasmoid formation. XOCOT has an added coaxial inner coil that assists in stabilizing the formation and compression processes. Typically, discharge frequencies of coaxial devices are an order of magnitude slower, ideally providing longer plasma refinement times and higher ionization fractions. Early models of the FARAD are similar to PIT designs with reference to geometry and method of discharge. However the form of propellant injection is substantially modified to allow for a pre-ionization (PI) stage to increase ionization fraction and thrust output. This PI stage also allows for FARAD to operate at much lower voltages during its main induction phase.

Pre-ionization of propellant gas can be a beneficial addition to the operation of a PIPA. Early FRC fusion studies showed that insufficient PI can lead to higher resistivities in formation plasma (which corresponds to a reduced plasma temperature) increasing instabilities and reducing fusion energy production.[1,16] Resistivity was able to be reduced by 45% when selective control of the timing and energy levels of the PI stage was enforced. Studies on the XOCOT showed that sufficient PI was imperative for forming a plasmoid.[8,17] More recently, results from the XOCOT-T have shown that pre-pre-ionization can aid formation. Finally, results from the FARAD device have shown that PI can lower the required discharge voltage for forming and accelerating the high-density current sheet produced by a PIPA. While PI is known to affect the overall performance and operation of PIPAs, studies focused on how to best implement or operate the PI stage are still lacking.

The following sections describe a numerical investigation of a pulsed inductive RF plasma source. The pulsed inductive RF plasma is envisioned as a PI source for a pulsed inductive accelerator and results from simulations are analyzed from this perspective. Specifically, we define the ion energy fraction as the fraction of total energy used to create ions and investigate how PI source characteristics, such as pulse duration, seed plasma density, and total energy addition, affect the ion energy fraction. Additionally, we consider how pre-ionization source characteristics affect peak ion density. First the global plasma model used for numerical simulations is described. Then simulation results are presented. Next, a detailed description of the PI source characteristics is presented, followed by discussion of the analysis. Finally conclusions and future work are presented.

II. Model Description

Modeling of inductive plasmas has met reasonable success with the primary goal of predicting plasma characteristics at the end of the induction phase to optimize efficiencies. Some have used numerical simulation to show theoretically that modulation of the induction profile can result in reduced ion production cost, higher ionization fraction, and increased plasma lifetime.[2,18,19] Others have used numerical analysis to study and optimize the induction phase of PIPAs.[20,21] Our approach is to slightly modify an existing, well-documented pulsed inductive RF plasma model and use it to study how PI source characteristics affect parameters that are important for a pulsed inductive accelerator, such as ion energy fraction, peak ion density, and optimum pulse timing. Therefore, an already-published, globally-averaged, time-resolved model is reproduced from Ref. 22 and modified for our problem statement. This model is derived from the methods outlined for steady state systems[23,24] and review of these and other techniques is also summarized in literature.[25] Developed with a focus on Argon gas (monatomic gas) this methodology proves comparatively simple against more computationally intensive particle-in-cell, MHD, or hybrid simulation codes.

A. Development of Rate Equations

Four coupled differential equations make up the bulk of the original model providing creation/decay rates of two excited species as well as electrons, and power distribution/losses (i.e., energy balance). For the analysis of focus

here, quantification of individual excited species is not necessary and is therefore consolidated to reflect an average excited species with excitation energy, ε_{ex}, of 12.14 volts. This reduces the model developed below to a system of three coupled differential equations. The generalized rate equation for the excited state is given by equation (1), which includes collisional creation/destruction rates, spontaneous decay to ground, and diffusion losses to the walls of a thin sheath cylinder.

$$\frac{dn_{ex}}{dt} = \sum_i K_i n_j n_k - K_{rad} n_{ex} - D_{eff} n_{ex} \left[\left(\frac{\pi}{L} \right)^2 + \left(\frac{2.405}{R} \right)^2 \right] \tag{1}$$

L and R are the length and radius of a characteristic cylindrical geometry (taken to be 7.5 cm and 15.25 cm, respectively, Ref. 22) and D_{eff} is an effective diffusion coefficient. Also, K_{rad} is taken to be a reduced effective Einstein coefficient, A_{eff}, as outlined in the appendix of Ref. 22. Rate constants used are given in Table 1. The effective diffusion coefficient is found by a combination of D_{AA^*} estimated from the Chapman-Enskog equation for like-particle diffusivity,[26] and of D_{KN}, a modified Knudsen free-diffusion coefficient.

$$D_{eff} = \frac{1}{(1/D_{AA^*} + 1/D_{KN})} \tag{2}$$

where D_{AA^*} and D_{KN} are given by,

$$D_{AA^*} = \frac{2}{3} \sqrt{\frac{(kT_0)^3}{\pi^3 m_A}} \frac{1}{p d_A^2} \quad \text{, and} \quad D_{KN} = \frac{v_{th}}{3\sqrt{\left(\frac{\pi}{L} \right)^2 + \left(\frac{2.405}{R} \right)^2}} \tag{3}$$

Here T_0 and m_A are the gas temperature (assumed constant) and mass associated with the species of interest (taken to be the initial neutral species). Pressure, p, is taken to be $n_i k T_0$ while d_A is the diameter of argon, approximately 1.42×10^{-10} m. Thermal velocity, v_{th}, is given by $(kT_0/m_A)^{1/2}$.

Table 1: Rate Constants for all reactions used in the modified model presented here.

Reaction	*Rate constant, K_i* (m^3/s)
Ar+e (elastic)†	$2.336 \times 10^{-14}\ T_e^{1.609} \exp[0.0618\ (\ln T_e)^2 - 0.1171 (\ln T_e)^3]$
Ar+e → Ar*+e†	$2.48 \times 10^{-14}\ T_e^{0.33} \exp[-12.78/T_e]$
Ar*+e → Ar+e‡	$6.88 \times 10^{-16}\ T_e^{0.33}$
Ar+e → Ar⁺+2e	$2.3 \times 10^{-14}\ T_e^{0.68} \exp[-15.76/T_e]$
Ar*+e → Ar⁺+2e	$9.34 \times 10^{-14}\ T_e^{0.64} \exp[-3.40/T_e]$
Reaction	*Einstein Coefficient, A_i* (s^{-1})
Ar* → Ar+$h\nu$§	$A_{eff} \approx 5.14 \times 10^5$

† *Source from Lieberman and Lichtenberg[27] valid in the range 1 to 7 eV.*

‡ *Estimated by detailed-balance analysis.*

§ *Reduced effective decay rate outlined in appendix of Ashida, Lee, and Lieberman.[22]*

Balance of electrons is given by equation (4) which includes ionization and recombination as well as losses to the walls.

$$V \frac{dn_e}{dt} = V \sum_i K_{iz,i} n_e n_i - n_e u_B \left[\frac{0.86(2\pi R^2)}{\sqrt{3 + \frac{L}{2\lambda_i}}} + \frac{0.80(2\pi R L)}{\sqrt{4 + \frac{R}{\lambda_i}}} \right] \tag{4}$$

Then, imposing a quasi-neutral assumption, rate of change of ions is also given by equation (4). Or mathematically,

$$V\frac{dn_{ion}}{dt}=V\frac{dn_e}{dt} \tag{5}$$

Loss to the walls in equation (4) is estimated by the original authors from analytical solutions presented by Godyak and Maximov for diffusion at the sheath edge. Volume, V, of the plasma also assumes a thin sheath meaning $V=\pi R^2 L$ and λ_i is the ion-neutral collision mean free path calculated by a Maxwellian electron distribution averaged over argon ionization cross-section data.[28] Assuming free diffusion of neutrals is negligible during the time-scales of interest (i.e., cold neutrals with no direct losses), then an additional rate equation for neutral species can be constructed from rate constants involving the excited and electron species.

Energy balance is achieved through equating total power absorbed from the pulsed device to the plasma (assumed known) to all loss and energy transfer mechanisms. Namely, species creation/destruction, loss to the walls, and overall electron temperature increases.

$$P_{\text{abs}}(t)=V\left[\frac{d}{dt}\left(\frac{3}{2}e\,n_e T_e\right)+e\,n_e\sum_i \varepsilon_i K_i n_j\right] + n_e u_B\left[\frac{0.86(2\pi R^2)}{\sqrt{3+\frac{L}{2\lambda_i}}}+\frac{0.80(2\pi R L)}{\sqrt{4+\frac{R}{\lambda_i}}}\right]\left(e\,V_s+\frac{5}{2}e\,T_e\right) \tag{6}$$

where P_{abs} is the total power input to the system as a function of time, ε_i and K_i are the energy and reaction rate constant, respectively, associated with the i^{th} reaction, n_j is the non-electron species involved in the reaction, and V_S is the sheath voltage drop given by

$$V_s=\frac{T_e}{2}\ln\left(\frac{M}{2\pi m}\right) \quad . \tag{7}$$

Known power absorbed is input via a positive-bias, square-wave pulse. The time derivative term is separated by the product rule and the set of differential equations (1), (4), and (6) are solved simultaneously via a MatLab solver.

B. Model Validation

For verification of agreement with reported results, test cases of 100 kHz, 10 kHz, and 1 kHz with 25% duty cycle and power of 2000 W are performed. Initial conditions (IC's) of each case are interpreted from graphs and reported data. These values are reproduced in Table 2. Background gas pressure and temperature are assumed constant. Figures 1 and 2 provide a side-by-side comparison of the reported results with current results of this work.

At this point, verification of the base model (and it's steady-state predecessor) with experiment is addressed by deference to previous works by other authors.[18,25] By extension then, the modified model outlined in this work reflects the species creation and composition trends found in a pulsed inductive RF plasma.

Table 2: Initial conditions for each case from Ref 22.

Case	*100 kHz*	*10 kHz*	*1 kHz*
Period (μs)	10	100	1000
Gas pressure (mTorr)	5	5	5
Gas temperature (K)	600	600	600
Total energy input (mJ)	5.0	50.0	500.0
Interpreted Initial Conditions			
n_{ground} (m^{-3})	8.0×10^{19}	8.0×10^{19}	8.0×10^{19}
n_{ex} (m^{-3})	1×10^{17}	0.0	0.0
n_{ion}, n_e (m^{-3})	2.5×10^{17}	3.0×10^{17}	1.0×10^{17}
T_e (eV)	1.0	0.5	0.5

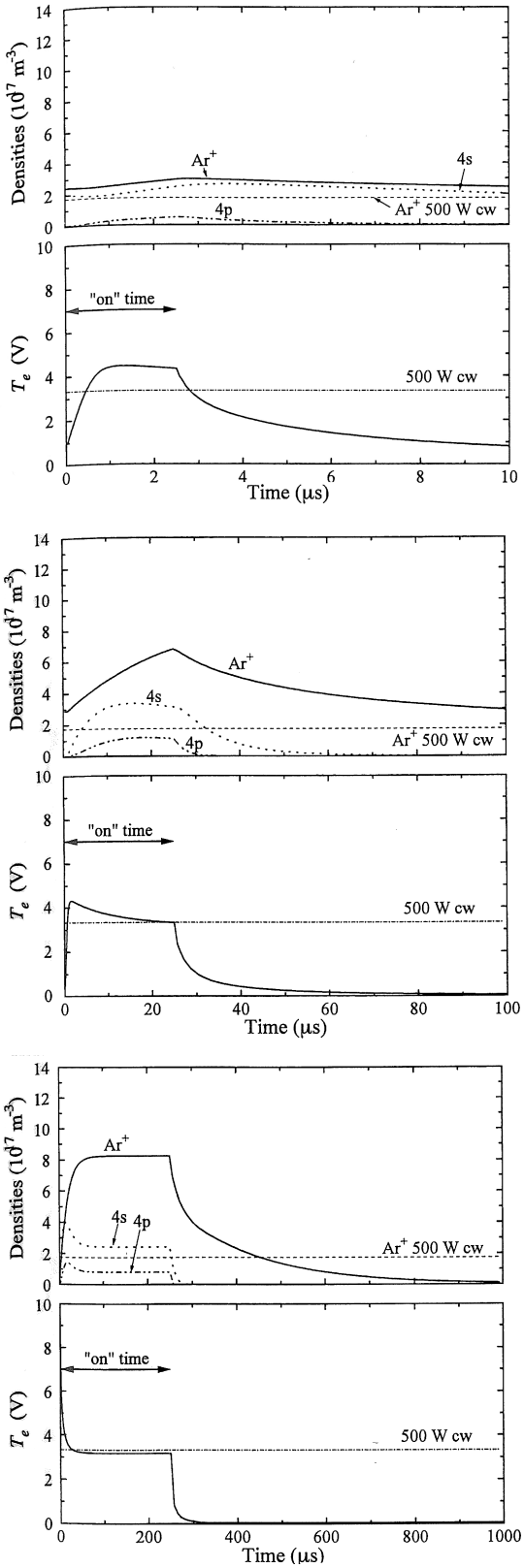

Figure 1: Reported results for 100 kHz, 10 kHz, and 1 kHz; 2000 W at 25% of cycle from Ref 22.

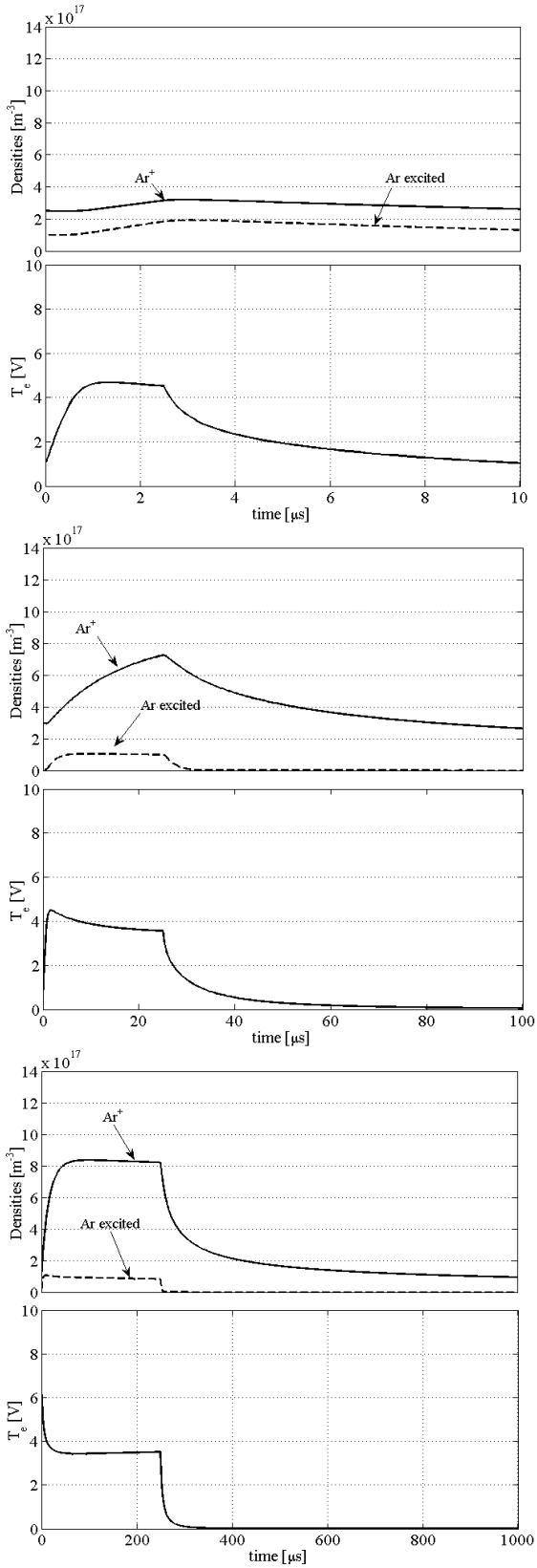

Figure 2: Reproduced results with single averaged excited species (work presented here)

III. Results

Simulations are performed for different energy input pulse duration, seed plasma density, and total deposited energy. Further description of these different test cases and simulation results are provided in the following sections. Results are plotted to show variation of plasma density, excited species density, and electron temperature versus time, as well as peak plasma density as a function of pulse duration, seed plasma density, and total deposited energy.

A. Variance in Pulse Duration

The baseline simulation is derived from the 100 kHz case of Table 2. Total energy deposited, initial charged and excited species densities, initial electron temperature, neutral gas temperature, and chamber geometry remain the same. Table 3 summarizes these characteristics. Table 3 also shows the different pulse durations investigated, and the corresponding power level. Because total energy deposited (5 mJ) is constant, as pulse duration decreases, power increases.

Table 3: Conditions for each variation in pulse duration.

Iter.	total energy	initial densities (m^{-3})			T_e	pulse duration (s)	power applied (kW)
		n_{ground}	n_{ex}	n_{ion}, n_e			
1						$3.33x10^{-6}$	1.50
2						$2.22x10^{-6}$	2.25
3						$1.48x10^{-6}$	3.38
4						$9.88x10^{-7}$	5.06
5						$6.58x10^{-7}$	7.59
6						$4.39x10^{-7}$	11.39
7						$2.93x10^{-7}$	17.09
8	5.0 mJ	$8.0x10^{19}$	$1.0x10^{17}$	$2.5x10^{17}$	1.0 eV	$1.95x10^{-7}$	25.63
9						$1.30x10^{-7}$	38.43
10						$8.67x10^{-8}$	57.67
11						$5.78x10^{-8}$	86.50
12						$3.85x10^{-8}$	129.75
13						$2.57x10^{-8}$	194.62
14						$1.71x10^{-8}$	291.92
15						$1.14x10^{-8}$	437.89

Figure 3 shows the density and electron temperature results for pulse durations of $3.33x10^{-6}$ seconds and $1.14x10^{-8}$ seconds. These were the longest and shortest pulse durations tested. For the shortest pulse duration, ion density initially increases reaching a peak of $3.7x10^{17}$ m^{-3} at 0.8 microseconds and then decreases. The longest pulse duration ion density slowly ramps up, achieving a peak of $3.1x10^{17}$ m^{-3} at 3.5 microseconds. Despite these different trends by the end of 5 microseconds densities for the two runs fall to within approximately 12% with the shorter pulse duration having higher density. Electron temperature initially increases and then decreases for both pulse durations. However, the temporal profiles are very different. Electron temperature for the shortest pulse duration increases quickly to 16 eV in about 0.05 microseconds and then quickly decays to less than 4 eV at 0.8 microseconds. Electron temperature for the longest pulse duration ramps up more slowly, reaching 4 eV at 0.8 microseconds and then remaining relatively constant at 4.5 eV from 1.1 to 3.2 microseconds before slowly decaying. At a time of 5 microseconds, final electron

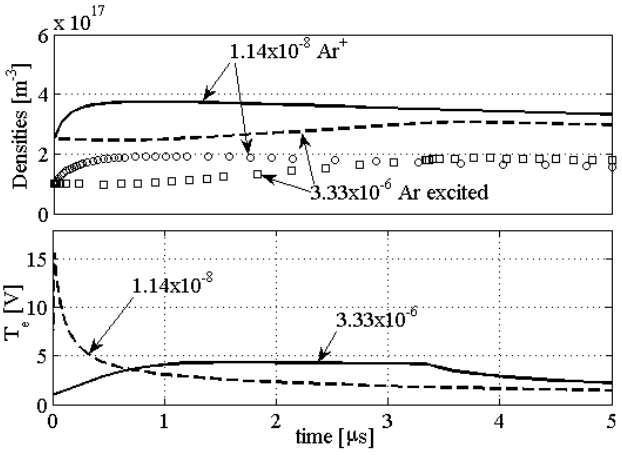

Figure 3: Results for variation of pulse duration highlighting the longest and shortest times tested. curves: ion densities, data points: excited densities

temperature for the short duration case is 35.5% less (at 1.43 eV) than that of the long duration case (at 2.218 eV).

The differences in the electron temperature and ion density profiles of Figure 3 are due to the input power, or the time over which energy is added to the plasma. As outlined in Table 3, total energy into the system is constant at 5.0 mJ for both cases. When energy is added to the electrons very quickly (shortest pulse duration), electron temperature spikes and then decays as ionization and diffusion processes slowly cool the electron population. High electron temperature at early time results in more energetic collisions and thus ion density also peaks early. When the energy is added slowly (longest pulse duration), electron temperature slowly increases and then reaches a plateau. This plateau is indicative of equilibrium, where energy is being added to the electron population at the same rate it is removed by ionization and diffusion processes. Over this time interval the ion density slowly grows. The discontinuity in the electron temperature at 3.33 microseconds corresponds with the end of the energy addition pulse. This can also be seen in the validation plots above (Figures 1 and 2) at 25% of each cycle period. When energy addition ends, the electron population cools, usually very abruptly.

Figure 4 shows the variation in peak ion and excited species densities with pulse duration. As pulse duration increases from 1.14×10^{-8} to 1.3×10^{-7} seconds, peak ion density decreases only 1% from its peak value of 3.7×10^{17} m^{-3}. Then peak ion density decreases an additional 9% to 3.4×10^{17} m^{-3} by 1.48×10^{-6} seconds. As pulse duration continues to increase, peak ion density decreases more rapidly, reaching a value of 3.1×10^{17} m^{-3} at the longest pulse duration tested of 3.33×10^{-6} seconds. From the shortest to longest durations, peak ion density drops by 18.3%. As pulse duration increases from 1.14×10^{-8} to 9.9×10^{-7} seconds, peak excited state density increases from 1.92×10^{17} m^{-3} to 1.99×10^{17} m^{-3}. Peak excited state density then decreases, reaching 1.86×10^{17} m^{-3} at the longest pulse duration. Over the entire range of pulse durations tested, excited state density varies by about 7%.

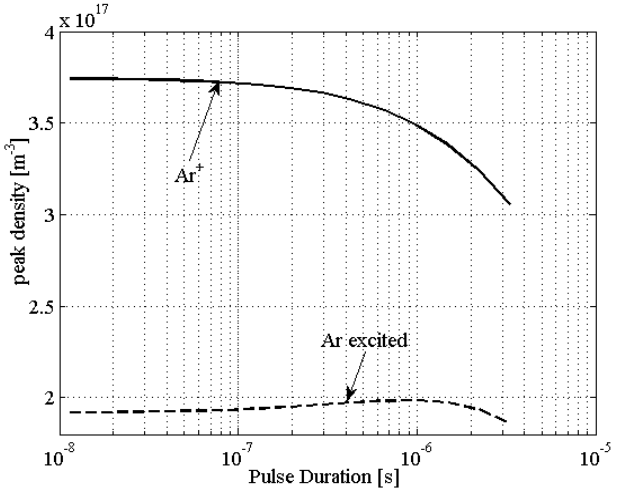

Figure 4: Peak densities for varying pulse duration.

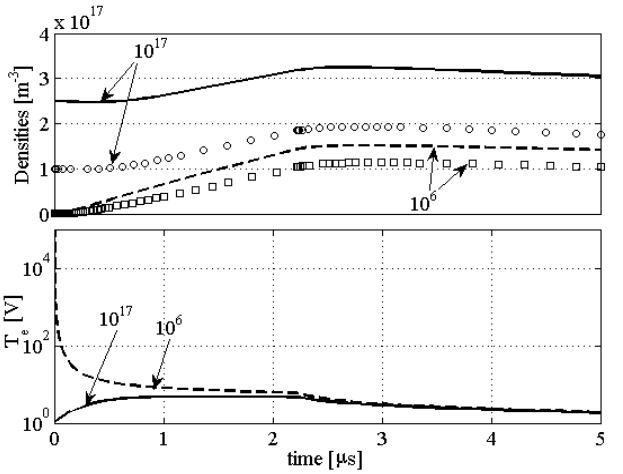

Figure 5: Results of variation in initial ion and excited species densities highlighting the smallest and largest density magnitudes. curves: ion densities data points: excited densities.

B. Variance in Seed Plasma Density

Effects of varying seed plasma density are investigated. Seed plasma density is the density of plasma present before the PI source is applied and is commonly referred to as pre-pre-ionization, or pre-PI. Simulations with different initial ion and excited state densities are conducted with density magnitudes ranging from 10^6 to 10^{17} m^{-3}. Iterations at every whole power of ten are listed along with the other primary simulation inputs in Table 4.

Figure 5 shows densities and electron temperature for varying seed density. Specifically, the two iteration limits of 10^6 m^{-3} (low density case) and 10^{17} m^{-3} (high density case) are shown. Densities for the high density case show a lag of about 0.5 microseconds behind the low density case before beginning to rise. Between 0.5 and 2.5 microseconds the ion density rise rate for the low and high density cases are 6.3×10^{16} and 4.6×10^{16} m^{-3} μs^{-1}, respectively, while excited state rise rates are both around 5.3×10^{16} m^{-3} μs^{-1}. Peak ion and excited densities for the low density case are 1.5×10^{17} and 1.1×10^{17} m^{-3}, respectively, and occur at 2.7 and 2.9 microseconds, receptively. Peak ion and excited densities for the high density case are 3.2×10^{17} and 1.9×10^{17} m^{-3}, respectively, and occur at 2.6

and 2.7 microseconds, respectively. These peak times occur just past the end of the energy input pulse at 2.22 microseconds. After pulse power shuts off, ion and excited states begin to decrease for both cases. At 5 microseconds the final ion density for the low density case is 54% lower (at $1.4x10^{17}$ m^{-3}) than the final ion density for the high density case (at $3.0x10^{17}$ m^{-3}). Final excited state density is 40% lower (at $1.0x10^{17}$ m^{-3}) for the low density case than the high density case (at $1.8x10^{17}$ m^{-3}). In the lower plot of electron temperature the low density case peaks nearly instantly at 99.5 keV, while the high density peaks at 4.8 eV at roughly 1.1 microseconds. Despite a stark contrast initially, final electron temperature between the two cases is within 4% at around 1.85 eV.

The electron temperature plot also highlights a prominent feature of low initial density. The electron temperature almost instantly reaches extremely high values of 100's of keV, then falls equally as rapid. This is partially a result of the ideal square-wave power input used. In real device operation output power in the form of an RF induction wave will have some small, but finite rise time associated with it and input to the charge carriers will require some time in addition to this. However, the very sharp and large electron temperature is primarily due to the very real condition of low initial density. As seen from equation (6) the absorbed input power is distributed to the number of charge carriers as electron temperature. If power is applied to a minimal number of charge carriers then the amount of energy distributed to each is quite large.

Figure 6 shows peak ion and excited state densities versus tested seed densities. Prominent in this plot is the constant ion and excited state peak densities of $1.51x10^{17}$ and $1.14x10^{17}$ m^{-3}, respectively, below approximately 10^{14} m^{-3} initial seed density. Above 10^{14} m^{-3} initial density, peak densities begin to increase as the initial densities approach the same order magnitude as peak densities. This trend eventually reaches a maximum at which point the energy added is insufficient to counter loss mechanisms and initial density becomes peak density as ion and excited levels decrease immediately in early times.

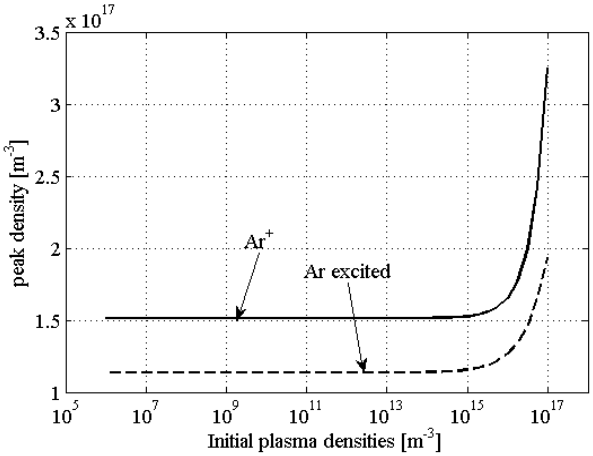

Figure 6: Peak densities for varying initial densities.

Table 4: Conditions for highlighted seed plasma density variations.

Iter.	total energy	initial densities (m^{-3})			T_e	pulse duration	power applied
		n_{ground}	n_{ex}	n_{ion}, n_e			
1	5.0 mJ	$8.0x10^{19}$	$1.0x10^{6}$	$2.5x10^{6}$	1.0 eV	$2.22x10^{-6}$ s	2.25 kW
5			$1.0x10^{7}$	$2.5x10^{7}$			
9			$1.0x10^{8}$	$2.5x10^{8}$			
13			$1.0x10^{9}$	$2.5x10^{9}$			
17			$1.0x10^{10}$	$2.5x10^{10}$			
21			$1.0x10^{11}$	$2.5x10^{11}$			
25			$1.0x10^{12}$	$2.5x10^{12}$			
29			$1.0x10^{13}$	$2.5x10^{13}$			
33			$1.0x10^{14}$	$2.5x10^{14}$			
37			$1.0x10^{15}$	$2.5x10^{15}$			
41			$1.0x10^{16}$	$2.5x10^{16}$			
45			$1.0x10^{17}$	$2.5x10^{17}$			

C. Variance in Total Energy Deposition

Variation of total input energy is also investigated. Energy input of 5.0 mJ is considered the baseline for comparison. Other simulation conditions are taken directly from the 100 kHz case in Table 2, except pulse duration is reduced from $2.5x10^{-6}$ seconds to $2.22x10^{-6}$ seconds to maintain consistency with the other studies presented here. All of these conditions are tabulated in Table 5 for reference.

Figure 7 shows the variation of densities and electron temperature for two cases, the 5 mJ (low energy) and 80 mJ (high energy) cases. Densities in the high energy case have a much higher rise rate in the early times (around 1 microsecond) of approximately $4x10^{17}$ m^{-3} per microsecond compared to nearly zero for the low energy case. When the power input shuts off at 2.2 microseconds, ion levels remain fairly constant for the remainder of the simulation, while excited states begin to show noticeable decay. This is recognized as a result of the difference between species lifetimes as governed by the rate constants. Particularly the spontaneous emission rate for excited state argon. Peak ion and excited densities for the low energy case are $3.2x10^{17}$ and $1.9x10^{17}$ m^{-3}, respectively, and occur at 2.6 and 2.7 microseconds, respectively. Peak ion and excited densities for the high energy case are $3.1x10^{18}$ and $1.3x10^{18}$ m^{-3}, respectively, and occur at 3.6 and 2.3 microseconds, respectively. Most of these peak times occur just past the power-off time of 2.22 microseconds except for the high energy ion case which is nearly 1.5 microseconds past power-off. In the lower plot of electron temperature the low energy case peaks to 4.8 eV at 1.15 microseconds and the high energy case at 12.1 eV at 0.2 microseconds. Despite large differences in initial trends, final electron temperature between the two cases is within about 8% at the end of the simulation at 5 microseconds, with the high energy case (1.7 eV) just below the low energy case (1.8 eV). It should be noted here that, similar to previous results, final densities are very different (90%), while final electron temperature is nearly identical.

Figure 8 shows peak densities as a function of total energy deposition. A nearly linear rise in peak ion density can be seen for increases in total energy reaching a peak of $6.6x10^{18}$ m^{-3}, while excited species plateau near $1.8x10^{18}$ m^{-3}.

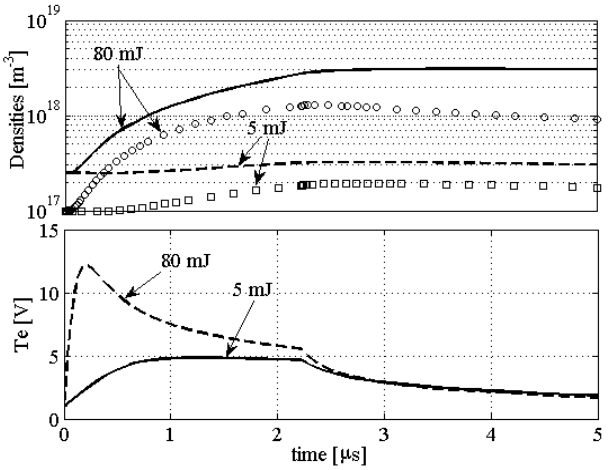

Figure 7: Results of variation in total energy deposition highlighting the 5 mJ and 80 mJ cases. curves: ion densities, data points: excited densities.

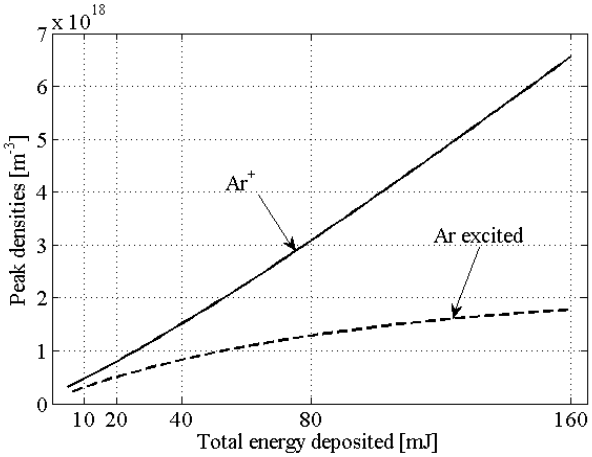

Figure 8: Peak densities for varying total energy deposition.

Table 5: Conditions for each increase in total energy deposition.

Iter.	total energy	initial densities (m^{-3})			T_e	pulse duration	power applied
		n_{ground}	$n_{excited}$	n_{ion}, n_{elec}			
1	5 mJ	$8.0x10^{19}$	$1.0x10^{17}$	$2.5x10^{17}$	1.0 eV	$2.22x10^{-6}$ s	2.25 kW
2	10 mJ						4.50 kW
3	20 mJ						9.00 kW
4	40 mJ						18.02 kW
5	80 mJ						36.04 kW
6	160 mJ						72.07 kW

IV. Analysis and Discussion

An analysis and discussion of plasma simulation results is presented in this section. Specifically, results are analyzed from the perspective of an EP propulsion system, assuming the pulsed inductive RF plasma is functioning as a PI stage for a pulsed inductive accelerator stage. In general, desirable PI plasma has low ion production cost and high density. First a description and rationale for the metrics of the analysis are described. Then these metrics are used to analyze the PI source characteristics: pulse duration, seed plasma density, and total energy deposition.

A. Analysis Metrics

A desirable PI plasma has high density and low ion production cost. The analysis metrics used in the following discussion are the peak ion density and the ion energy fraction. In all cases peak ion density corresponds with peak ionization fraction. The ration ale for these metrics is described below.

Common analyses of electric propulsion systems[29] define thrust-to-power ratio and effective exhaust speed as,

$$\frac{T}{P_{elec}} = \frac{2\eta_t}{g_0 I_{sp}} \quad \text{and} \quad v_e = \frac{T}{\dot{m}} = \frac{I_{sp}}{g_0} \tag{8}$$

where T, P_{elec}, η_t, g_0, and I_{sp} are the thrust, total electrical input power, thruster efficiency, Newton's constant, and specific impulse, respectively. Substituting the definition for efficiency, equation (8) can be manipulated to define thrust as,

$$\eta_t \stackrel{\text{def}}{=} \frac{1}{2}\dot{m} v_e^2 \frac{1}{P_{elec}} \quad \rightarrow \quad \boxed{T = \frac{\dot{m} v_e^2}{g_0 I_{sp}}} \tag{9}$$

where $\dot{m}$ and v_e^2 are the mass flow rate and effective exhaust speed, respectively. Assuming effective exhaust speed, and hence I_{sp}, and spacecraft power are constant, the simple analysis provided by equation (9) shows the dependence of thrust on the accelerated mass flow. The lynch-pin of this statement is that the mass accelerated and ejected from the device consists only of *ionized* species. This means un-ionized particles are either not accelerated or are dragged along during the acceleration process due to viscous forces (reducing the effective momentum transferred to the vehicle). Therefore achieving a PI plasma state with the maximum number of ions is desirable, and the first metric is peak ion density.

For a given EP system input electric power, P_{elec}, a power balance analysis of the device yields,

$$P_{elec}\, dt = E_T + E_{ion} + E_{rad} + E_{loss} + E_{therm} \tag{10}$$

where E_T, E_{ion}, E_{rad}, E_{loss}, and E_{therm} are the energy totals partitioned out to thrust, ionization, radiation, other loss mechanisms, and overall heating of the gas, respectively. Efficient thruster design drives the necessity for E_T to be large relative to all other terms, while still recognizing the necessity for E_{therm} and E_{ion} to produce the plasma that is accelerated. However, E_{ion}, E_{rad}, E_{loss}, and E_{therm} should all be minimized for a given accelerated plasma plume density to reflect a low ion production cost.

In a PI plasma, input energy heats the gas, produces ions, and is lost via radiation and diffusion to the walls. This can be expressed as equation (11).

$$P_{abs}\, dt = E_{ion} + E_{rad} + E_{walls} + E_{therm} \tag{11}$$

As the plasma evolves over time, as seen in Figures above, energy is converted between these different forms. For instance, energy is initially deposited into thermal electron energy, where it is used to produce ions and excited species. Energy is then lost when excited species emit line radiation and ions and electrons diffuse to the wall. To achieve the lowest ion production cost, the PI plasma should be ejected when the ion energy fraction is highest. Ion energy fraction is

$$ion\ energy\ fraction \stackrel{\text{def}}{=} \frac{E_{ion}}{E_{tot}} = \frac{V n_{ion} e \varepsilon_{iz}}{P_{abs}\, dt} \quad . \tag{12}$$

The ion energy fraction is the second metric used for analysis here. The denominator equals the total power absorbed up to time dt. This is key to the information this ratio conveys because it includes not only the energy tied to the charged and excited species but also any and all lost forms of energy up through time dt.

In the following sections, the two metrics of peak number density and ion energy fraction are used to evaluate the characteristics of the PI plasma source. Specifically, the effect of pulse duration, initial seed density, and total energy deposition is evaluated. Power duration of an RF source can be easily tuned by adjustment of circuit parameters and antenna geometry or in many cases is directly tunable on an amplified frequency generator. Seed

electron densities are generated by high voltage, steady state electrodes far up-stream of the induction chamber and their output is directly proportional to the voltage applied. Total absorbed energy is not directly controlled, but represents a measure of the overall power scalability of the PIPA device.

B. Pulse Duration

Ion energy fraction is plotted in Figure 9 and shows an increase of 19% from the longest to shortest pulse duration. Specifically, ion energy fraction is 15% and 34% for the longest and shortest pulse durations, respectively. Ion energy fraction remains high (33.5%) out to 1.3×10^{-7} seconds, then decreases in the same manner as peak ion density in Figure 4. Put another way, analysis of Figures 4 and 9 shows that for all other conditions being equal as outlined in Table 3, reducing pulse duration time by a factor of 100 (from 10^{-6} to 10^{-8} seconds) yields a gain of almost 19% in total energy stored in ions while simultaneously increasing peak ionization density by roughly 25%. Even a more modest decrease of a factor of 10 (from 10^{-6} to 10^{-7} seconds) yields a gain of approximately 16.5% ion energy fraction and keeps nearly a 25% increase in peak ion density.

Timing is critical in any pulsed power application, especially in inductive plasma thrusters. When varying the delay between pre-ionization and a main induction phase, delays on the order of microseconds have shown significant differences in plasma formation (and, by extension, thruster performance). So then, not only is a higher ion energy fraction important but the time at which that peak ratio occurs is also important because this is the optimum time to eject the plasma (i.e. when the device has reached the most ions for the least energy lost). To investigate this further, the time at which the peak ion energy fraction is reached is plotted in Figure 10 versus pulse duration. Some slight discontinuities in this plot can be seen which are a result of the tolerances used in the iterative differential equation solving process. Figure 10 shows that for a reduction in pulse duration from 3×10^{-6} to 3×10^{-7} the optimum firing time is reduced from just over 3.5 microseconds to just over 1 microsecond. And just as for ion energy fraction and peak densities, Figure 10 shows that pulse durations below about 200 nanoseconds yield little benefit.

C. Seed Plasma Density

Figure 11 shows ion energy fraction versus initial plasma densities. This plot conveys that seed plasma density has little effect when utilizing a fixed input power until densities within a few orders of magnitude of final ion density are used. One interesting trend is that a peak of around 41.8% in ion energy fraction remains up to initial densities of around 10^{15} m^{-3}, then falls off rapidly until reaching 20.62% at 10^{17} m^{-3}. This suggests that a low seed density is actually desired to keep ion energy fraction at peak.

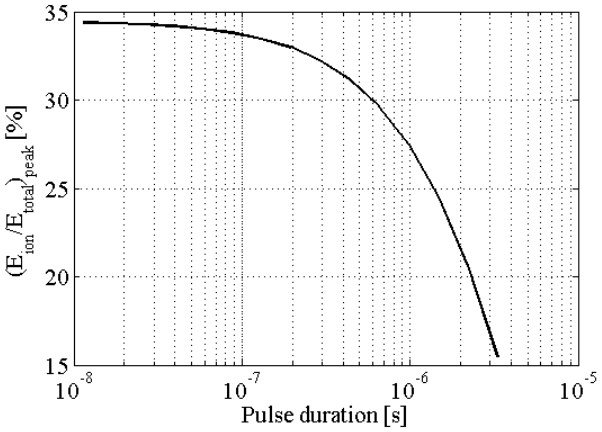

Figure 9: Peak ion energy fractions and species densities for varied pulse durations.

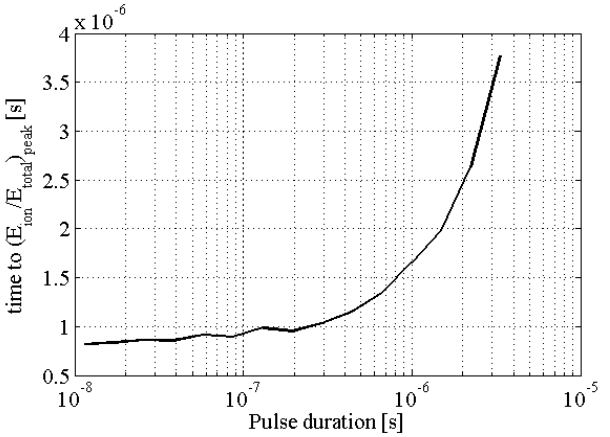

Figure 10: Time to reach peak ion energy fraction shown in Figure 9 occurs.

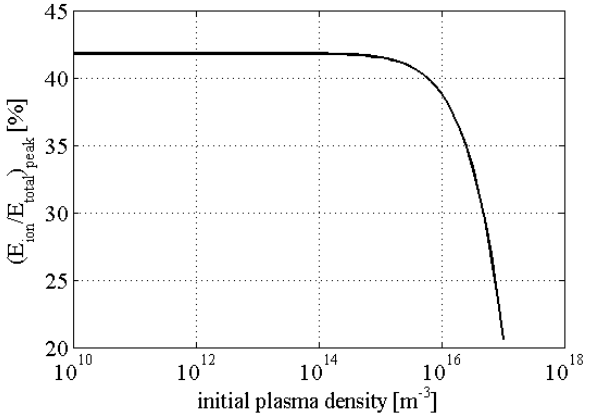

Figure 11: Peak ion energy fractions and species densities for variation of initial species densities.

D. Total Energy Deposition

Available energy and power (the rate at which the available energy can be delivered) are the key factors in any space vehicle's capability and mission flexibility. So making the most of that power is critical to device design. In this section several energies, over a wide range of power levels are compared against the results of pulse duration modulation. Figure 7 shows that upon increasing input energy by a factor of 2^4, or 16 (5 mJ to 80 mJ) the final ion density increases by only a factor of 10 ($3x10^{17}$ to $3x10^{18}$ m^{-3}). Relating this to Figure 9 shows that reduction of the pulse duration, which corresponds to an increase in necessary power, provides an increase in effective energy usage for ion production. Figures 12, 13, and 14 quantify the trade-offs of between increasing input energy and increasing power required.

Figure 12 shows peak ion density versus pulse duration for multiple total energy inputs. The high energy case of 160 mJ yields a peak ion density of $7.01x10^{18}$ m^{-3} at $2.9x10^{-7}$ seconds pulse duration. The low energy case of 5 mJ yields a peak ion density of $3.7x10^{17}$ m^{-3} at the shortest duration time of $1.14x10^{-8}$ seconds. This illustrates that highest peak density does not occur at the same pulse duration for each energy case. It occurs at the shortest duration for the low energy (5 mJ) case and then highest peak ion density shifts to longer durations as input energy increases. Also seen in Figure 12 is that as input energy increases the rate of decrease in peak ion density (past pulse durations of 10^{-6} seconds) becomes more pronounced. To estimate this, taking the two longest duration points for the high energy (160 mJ) case a decay rate of $2.7x10^{16}$ m^{-3} μs^{-1} loss in peak ion density is obtained. This means that at pulse durations of 10^{-6} and longer, for 160 mJ energy input, the peak ion density decreases by $2.7x10^{16}$ m^{-3} for every microsecond increase in pulse duration. By contrast, the same two points for the next highest energy (80 mJ) case yields a decay rate of $9.1x10^{15}$ m^{-3} μs^{-1}. Peak ionization at $3.3x10^{-6}$ seconds pulse duration is the lowest for that energy at $6.3x10^{18}$ m^{-3}. The 160 mJ energy case at peak ($7.01x10^{18}$ m^{-3}) density constitutes about an 8.8% total ionization fraction of the background argon gas. This was the highest ionization fraction encountered over all results.

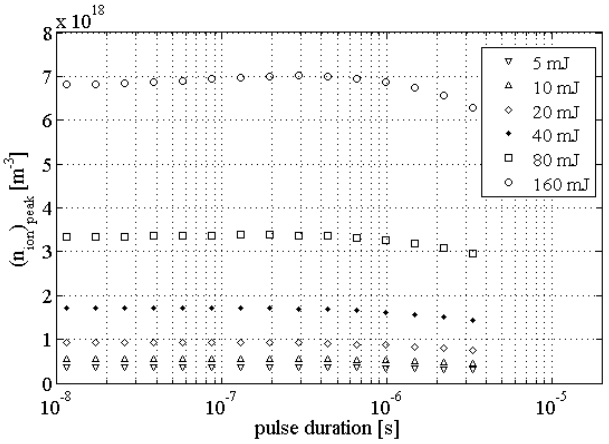

Figure 12: Peak ion densities for multiple deposit energies and pulse durations.

Figure 13 shows ion energy fraction versus pulse duration for the six energy cases. These ion energy fractions also have a shifting peak similar to the peak ion density plot of Figure 12 where the peak moves to longer duration times for higher energies. The 160 mJ case peaks to 58.4% at $2.9x10^{-7}$ seconds, the same duration time that peak ion density occurrs for this energy (from Figure 12). In contrast to Figure 12, as input energy increases the rate of decrease in ion energy fraction becomes *less* pronounced. Similar to the above analysis, to illustrate this data points at the two longest pulse durations are once more used to obtain a decay rate. For ion energy fraction, the low energy case exhibits the greatest decay rate at 4.7% μs^{-1}. To clarify, this means that at pulse durations of 10^{-6} and longer, for 5 mJ energy input, the peak ion energy fraction is reduced by 4.7% for every microsecond increase in pulse duration. By contrast, the high energy case is only 2.1% μs^{-1}. Additionally it is noticed that as energy input increases,

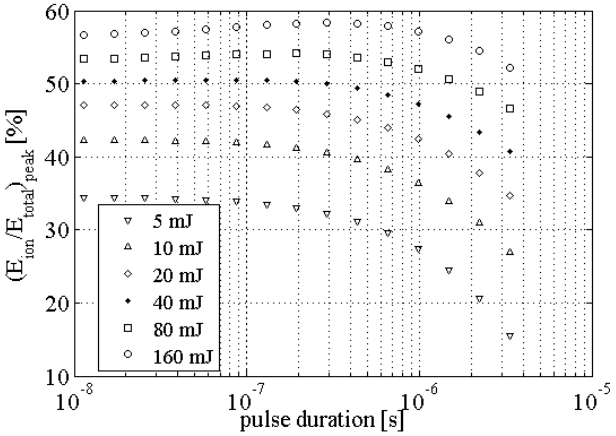

Figure 13: Peak ion energy fraction for multiple total deposit energy and pulse durations.

the peak ion energy fraction increases. Simply put, this means that as larger energies are put into the system more energy is going into ion production than either losses or excited state atoms or both. Also this plot shows that the amount of increase diminishes each time input energy is doubled. Exactly what this limit is remains to be seen but appears to be near 60% to 65%. The energy limit of 160 mJ is considered a very high limit because 160 mJ at a pulse duration of 1.14×10^{-8} seconds yields a power level of around 14 MW which is orders of magnitude higher than any current EP spacecraft power plant to date.

Figure 13 also makes it straightforward to see multiple energy points that share a peak in ion energy fraction. For example a point on the 40 mJ data series in Figure 13 shows an ion energy fraction peak of 40.8% with a pulse duration of 3.33×10^{-6} seconds while a point on the 10 mJ data series shows nearly the same ion energy fraction peak at 40.5% with a pulse duration of approximately an order of magnitude less at 2.93×10^{-7} seconds. While both provide the same ion energy fraction, the latter uses 75% less total energy at the cost of a higher power (12 kW versus 34.2 kW) and has a 67% reduction in peak ion density. Mitigation of this loss in peak ion density while maintaining a lower power warrants further investigation.

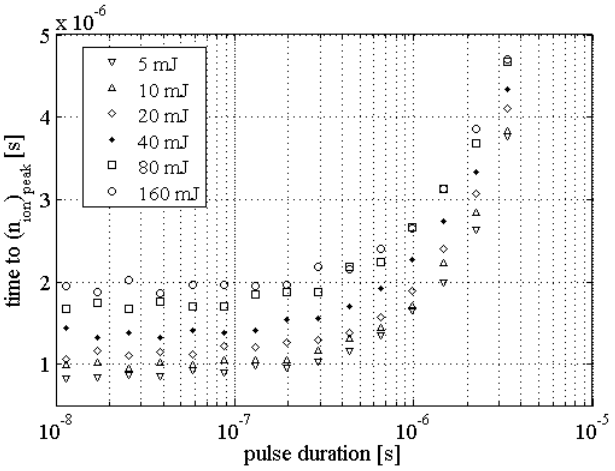

Figure 14: Time to reach peak ion density for multiple total deposit energy and pulse durations.

Figure 14 shows the time to reach peak ion density versus pulse duration for the six energy cases. As with the single energy case above the time at which the peak occurs remains almost constant at durations of less than about 200 nanoseconds for all energy cases. Minimum time does vary from lowest to highest energies with a minimum of approximately 0.82 microseconds for the low energy, 5 mJ case, and approximately 2.0 microseconds for the high energy, 160 mJ case. Revisiting Figure 12 it is seen that the exponential increase in input energy also has an exponential increase in peak ion density. Therefore the trend of Figure 14 showing an increase in time to peak for increased input energies is attributed to the fact that making more ions by the same reaction mechanisms takes longer.

V. Conclusions

In conclusion the modeling results presented here show that an increase in energy stored in ions can be achieved while simultaneously reducing the energy diverted to loss mechanisms by manipulation of pulse duration time, initial seed plasma density, and total energy deposition. The ion energy fraction is defined to better describe the percentage of energy that the ionization fraction represents as it relates to the total energy lost in the plasma formation process. Adjustment of pulse duration alone shows to increase the percentage of total input energy entrained in ions by 16.5% by reducing duration time from 10^{-6} to 10^{-7} seconds. Seed plasma density has the smallest effect on ion energy fraction holding at 41.8% until densities at or near final ion densities are employed. At which point ion energy fraction begins to decrease rapidly. These results suggest that a low seed plasma density is actually preferred over those near final expected densities. Increases in total energy deposited appear to increase the percentage of total input energy entrained in ions. However this trend appears to diminish near 65% as energy increases exponentially. Analysis also provides some quantifiable insights into the trade-offs between low power, high energy systems versus a high power, low energy systems showing that the same peak ion energy fraction can be achieved (about 40.6%) for power levels ranging from 12 kW to 34 kW.

VI. Future Work

Further investigations adjusting initial neutral background gas density and/or additional input energy (at lower powers) is necessary to adequately test the results and postulations developed here at, or near, 100% ionization conditions. Additionally, adjustment of geometry, initial conditions, and prescribed power (in both magnitude and

time-domain profile) will be undertaken to reflect those of the Missouri Plasmoid Experiment (MPX) which is an FRC test article sponsored by the Air Force Office of Scientific Research.[30] Results from this analysis will be compared with experiment and further adjustments to the model may be made to more accurately reflect MPX conditions. Upon reasonable agreement with experiment this model will provide good, time-resolved, estimations of various energy transport mechanisms involved in the pre-ionization and early formation stages of a PIPA.

VII. Acknowledgments

The authors would like to thank the Missouri Research Board and the Air Force Office of Scientific Research (grant FA9550-10-1-0204) for helping to make this research possible.

References

[1] Tuszewski, M., "Field reversed configurations," *IAEA - Nuclear Fusion*, Vol. 28, No. 11, 1988, pp. 2033-2092

[2] Samukawa, S., & Mieno, T., "Pulse-time modulated plasma discharge for highly selective, highly anisotropic and charge-free etching," *IOP - Plasma Sources Sci. Technol.*, Vol. 5, 1996, pp. 132-138

[3] Brown, D.L., Beal, B.E., & Haas, J.M., "Air force research laboratory high power electric propulsion technology development," *Public Release*: Edwards AFB, CA, No. 2-0102, AFRL, 2009

[4] Armstrong, W.T., Cochrane, J.C., Commisso, R.J., Lipson, J., & Tuszewski, M., "Theta-pinch ionization for field-reversed configuration formation," *AIP - Appl. Phys. Lett.*, Vol. 38, No. 9, 1981, pp. 680-682

[5] Dailey, C.L., & Lovberg, R.H., "The PIT MkV pulsed inductive thruster," *Contractor Report*: Lewis Research Center, No. 191155, National Aeronautics and Space Administration, 1993

[6] Meyer, M., Johnson, L., Palaszewski, B., Goebel, D., White, H., & Coote, D., "In-space propulsion systems roadmap," *Tech Report*: NASA Headquarters, Washington, D.C. 20546, National Aeronautics and Space Administration, 2010

[7] Hopwood, J., "Review of inductively coupled plasmas for plasma processing," *IOP - Plasma Sources Sci. Technol.*, Vol. 1, 1992, pp. 109-116

[8] Kirtley, D.E., "Study of the synchronous operation of an annular field reversed configuration plasma device," University of Michigan, Dept. of Aerospace Engineering, 2008

[9] Russell, D., Poylio, J.H., Goldstein, W., Jackson, B., Lovberg, R., & Dailey, C.L., "The Mark VI pulsed inductive thruster," *Space Conference and Exhibit*, American Institute of Aeronautics and Astronautics, San Diego, California, 2004

[10] Polzin, K.A., "Scaling and systems considerations in pulsed inductive plasma thrusters," *IEEE - Transactions on Plasma Science*, Vol. 36, No. 5, 2008, pp. 2189-2198

[11] Polzin, K.A., "Comprehensive review of planar pulsed inductive plasma thruster research and technology," *AIAA - J. Propuls. Power,* 2008, *pending publication*

[12] Frisbee, R.H., & Mikellides, I.G., "The nuclear-electric pulsed inductive thruster (NUPIT): mission analysis for prometheus," *41st Joint Propulsion Conference and Exhibit*, AIAA, Tucson, AZ, 2005

[13] Koelfgen, S.J., & Hawk, C.W., "A plasmoid thruster for space propulsion," *39th Joint Propulsion Conference and Exhibit*, AIAA, Hustsville, AL, 2003

[14] Slough, J., Kirtley, D., & Weber, T., "Pulsed plasmoid propulsion: the ELF thruster," *International Electric Propulsion Conference*, ERPS, Ann Arbor, Michigan, 2009

[15] Choueiri, E.Y., & Polzin, K.A., "Faraday acceleration with radio-frequency assisted discharge," *AIAA - J. Propuls. Power*, Vol. 22, No. 3, 2006, pp. 611-619

[16] Steinhauer, L.C., Milroy, R.D., & Slough, J.T., "A model for inferring transport rates from observed confinement times in field-reversed configurations," *AIP - Physics of Fluids*, Vol. 28, 1985, pp. 888-897

[17] Niemela, C.S., & Kirtley, D., "Initial results on an annular field reversed configuration plasma translation experiment," *Report*: AFRL Edwards, CA, AFRL, 2008

[18] Ashida, S., Shim, M.R., & Lieberman, M.A., "Measurements of pulsed-power modulated argon plasmas in an inductively coupled plasma source," *AVS - J. Vac. Sci. Technol.*, Vol. 14, No. 2, 1996, pp. 391-397

[19] Sakuta, T., Oguri, S., Takashima, T., & Boulos, M.I., "Effects of plasma diameter and operating frequency on dynamic behavior of induction thermal plasma," *IOP - Plasma Sources Sci. Technol.*, Vol. 2, 1993, pp. 67-71

[20] Niemela, C.S., & King, L.B., "Numerical optimization of an annular field reversed configuration translation experiment," *International Electric Propulsion Conference*, Univ. of Michigan, Ann Arbor, MI, 2009

[21] Milroy, R.D., & Brackbill, J.U., "Numerical studies of a field-reversed theta-pinch plasma," *AIP - Physics of*

Fluids, Vol. 25, 1982, pp. 775-783
[22] Ashida, S., Lee, C., & Lieberman, M.A., "Spatially averaged (global) model of time modulated high density argon plasmas," *AVS - J. Vac. Sci. Technol.*, Vol. 13, 1995, pp. 2498-2507
[23] Lee, C., Graves, D.B., Lieberman, M.A., & Hess, D.W., "Global model of plasma chemistry in a high density oxygen discharge," *ECS - J. Electrochem. Soc.*, Vol. 141, No. 6, 1994, pp. 1546-1555
[24] Lee, C., & Lieberman, M.A., "Global model of Ar, O_2, Cl_2, and Ar/O_2 high-density plasma discharges," *AVS - J. Vac. Sci. Technol.*, Vol. 13, No. 2, 1995, pp. 368-380
[25] Lieberman, M.A., & Ashida, S., "Global models of pulse-power-modulated high-density, low-pressure discharges," *IOP - Plasma Sources Sci. Technol.*, Vol. 5, 1996, pp. 145-158
[26] Bird, R.B., Stewart, W.E., & Lightfoot, E.N., "Transport phenomena," 1st ed., 1960, p. 511
[27] Lieberman, M.A., & Lichtenberg, A.J., "Principles of plasma discharges and materials processing," 2nd ed., 2005, p. 134
[28] Rapp, D., & Englander-Golden, P., "Total cross sections for ionization and attachment in gases by electron impact. i. positive ionization," *AIP - J. Chem. Phys.*, Vol. 43, 1965, pp. 1464-1479
[29] Sutton, G.P., & Biblarz, O., "Rocket propulsion elements," 8th ed., 2010,
[30] Pahl, R.A., Meeks, W.C., & Rovey, J.L., "Characterization of preionization phase of a FRC test article," *47th Joint Propulsion Conference and Exhibit*, AIAA, San Deigo, CA, to be published